On Feature Motion Decorrelation in Ultrasound Speckle Tracking

Tianzhu Liang*, *Student Member, IEEE*, Lingsing Yung, *Student Member, IEEE*, and Weichuan Yu, *Member, IEEE*

Abstract—Speckle tracking methods refer to motion tracking methods based on speckle patterns in ultrasound images. They are commonly used in ultrasound based elasticity imaging techniques to reveal mechanical properties of tissues for clinical diagnosis. In speckle tracking, feature motion decorrelation exists when speckle patterns are not identical before and after tissue motion and deformation. Feature motion decorrelation violates the underlying assumption of most speckle tracking methods. Consequently, the estimation accuracy of current methods is greatly limited. In this paper, two types of speckle pattern variations, the geometric transformation and the intensity change of speckle patterns, are studied. We show that a coupled filtering method is able to compensate for both types of variations. It provides accurate strain estimations even when tissue deformation or rotation is extremely large. We also show that in most cases, an affine warping method that only compensates for the geometric transformation is able to achieve a similar performance as the coupled filtering method. Feature motion decorrelation in B-mode images is also studied. Finally, we show that in typical elastography studies, speckle tracking methods without modeling local shearing or rotation will fail when tissue deformation is large.

Index Terms—Elasticity imaging, feature motion decorrelation, speckle pattern variation, speckle tracking, ultrasound image analysis.

I. INTRODUCTION

IN LITERATURE, speckle tracking methods are usually referred to as motion tracking methods based on specific image patterns called speckles in ultrasound images [1]. Such methods to reveal the object motion of interest in ultrasound images have superior advantages against the traditional tissue Doppler imaging technique in that they provide all components of tissue motion in 2-D or 3-D, while Doppler imaging can only measure the motion along the beam direction (i.e., along the direction of ultrasound wave propagation) with a relatively lower resolution. Speckle tracking methods are often used in ultrasound based elasticity imaging [2], where two images of tissues before and after a specific motion and deformation are recorded and used for tissue motion inference. The specific tissue motion and deformation is revealed either in the spatial-temporal domain [3]–[6] or in the spectral domain [7], [8]. The mechanical properties of tissues are then inferred, which have been demonstrated to have high correlation with pathological changes of tissues [9]. For example, cancerous tissues typically have a tenfold higher stiffness of normal tissues because the structural organization of cells have changed. In liver cirrhosis, the stiffness of liver tissues increases dramatically due to fibrosis. In cardiac ischemia, dead heart tissues due to the lack of blood supply are stiffer than normal myocardial tissues.

In speckle tracking, feature motion decorrelation mainly refers to the cases when speckle patterns in ultrasound images are not invariant before and after tissue motion and deformation. It occurs when tissues undergo certain types of motion and deformation (e.g., compression, expansion, shearing, rotation, etc.). In such a situation, the underlying assumption of traditional motion tracking methods is violated. For instance, speckle patterns are distorted under some tissue deformation or rotation [10]. What is worse, the interference of backscattered ultrasound waves is changed, causing an intensity change in the speckle patterns. Such an intensity change violates the assumption of brightness constancy constraint equation (BCCE) [11], [12], which is the basis of most motion tracking methods. In general, speckle tracking methods will fail with large feature motion decorrelation.

In order to reduce feature motion decorrelation, a high-frame-rate imaging system has been proposed [13], [14]. Typically for 2-D ultrasound systems, a frame rate of more than 100 frames per second can be achieved. When an ECG gating technique is used, a much higher frame rate can also be achieved if one assumes that the cardiac motion is the same in different acquisitions. With such a high-frame-rate system, speckle patterns are almost identical for reliable matching. However, when out-of-plane motion occurs and no perfect match is available, the estimation accuracy of speckle tracking methods will be greatly limited. For 3-D ultrasound imaging systems, such a high-frame-rate system is not easy to achieve. Although the ECG gating technique can also help increase the frame rate of the 3-D imaging system, it has difficulty when the patient does not have identical cardiac motion in different acquisitions. Therefore, feature motion decorrelation cannot be avoided in some applications. More importantly, the technical problem remains unaddressed.

In order to address feature motion decorrelation, additional constraints have been incorporated in the search of motion parameters. For example, a Markov random field (MRF) model has been used to model the tissue motion, which assumes that

neighboring tissues have similar displacements [15]–[17]. Another example is the deformable model [18]–[22], which assumes that the tissue motion at different spatial positions can be interpolated from the motion of a few controlling points. A finite element method has also been proposed for the strain estimation [23]. A tissue incompressibility constraint has been used in literature [24], in which the volume of tissues is assumed to be constant during tissue motion and deformation. Estimation accuracy has been increased by using such techniques. However, these methods will fail when decorrelation is large, since feature motion decorrelation still exists. A correlation coefficient filtering method using a small window size has also been proposed to reduce the decorrelation in the correlation window [4]. However, the decorrelation cannot be completely eliminated.

Another solution of feature motion decorrelation is to compensate for the variations of speckle patterns between the pair of ultrasound images. For instance, in a local area speckle patterns are assumed to undergo some geometric transformation as the underlying tissues. The compensation of decorrelation is achieved by applying an inverse transformation to the distorted speckle patterns. Representative examples include the temporal stretching method for 1-D compression and expansion [25], [26] and the companding method for 2-D/3-D compression and expansion [27], [28]. In these methods, decorrelation has been reduced dramatically. However, the compensation is not complete and the estimation accuracy still suffers from the decorrelation when tissue deformation is large [29].

Recently, a coupled filtering method has been proposed [30]. Two different types of speckle pattern variations are treated. The first type of variation is the geometric transformation of speckle patterns caused by the underlying tissue motion and deformation. The second type of variation is the intensity change caused by the different interference of the reflected ultrasound waves after tissue motion and deformation. Both theoretical proof and experimental results show that the coupled filtering method is able to compensate for these two types of speckle pattern variations, even when tissue deformation or rotation is extremely large. However, it should be noted that the coupled filtering method cannot compensate for other types of speckle pattern variations, for example, the intensity change due to the variation of the point spread functions (PSFs) at different spatial positions. Besides, the coupled filtering method generally requires a longer computational time than traditional methods because of the increased number of motion parameters and the complex procedures for variation compensation. More importantly, the coupled filtering method is restricted to radio-frequency (RF) ultrasound images, which are generally not available in clinical practice.

In this paper, we demonstrate that speckle pattern variations under locally affine tissue motion can be treated properly by the coupled filtering method, even when tissue deformation or rotation is extremely large. We show that almost all speckle pattern variations can be explained by the two types of variations mentioned above. Besides, we demonstrate that in most cases, an affine warping method that only compensates for the geometric transformation of speckle patterns, is good enough for handling feature motion decorrelation. Such a method does not compensate for the intensity change of speckle patterns and
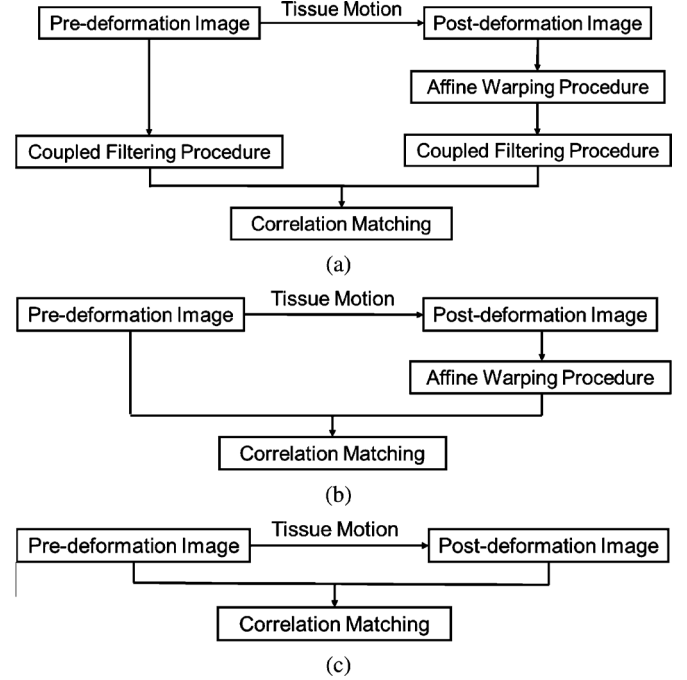

Fig. 1. Essential components of the coupled filtering method, the affine warping method, and the direct correlation method used in this paper. (a) The coupled filtering method with an affine warping procedure and a coupled filtering procedure before correlation matching. (b) The affine warping method with an affine warping procedure before correlation matching. (c) The direct correlation method. The affine warping procedure is able to compensate for the geometric transformation of speckle patterns, while the coupled filtering procedure is able to further compensate for the intensity change of speckle patterns.

is not restricted to RF ultrasound images. Therefore, feature motion decorrelation can be addressed in both RF and B-mode (BM) images. Finally, we show that for an elastography study where a quasi-static compression of tissues is applied, a tissue motion model with local translation, compression, expansion, shearing and rotation is necessary. Speckle tracking methods that do not model shearing and rotation (e.g., the companding method in [27], [28]) will fail when tissue deformation is large. Fig. 1 shows the relationship between the coupled filtering method, the affine warping method and the direct correlation method.

The remaining parts of the paper are organized as following: Section II explains theoretical foundations of the coupled filtering method and the affine warping method, as well as their relationships to other methods. Section III describes the implementation of these methods. Section IV presents the comparative study on the compensation for different types of variations. Section V studies feature motion decorrelation and its effects on strain estimations in BM images. Section VI compares speckle tracking methods with and without shearing and rotation modeling parts in a typical elastography study. Section VII concludes the paper with discussions.

II. THEORY

All methods in this section are described in the 3-D space. Without the lost of generality, we define that the beam direction, along which ultrasound waves are transmitted, is aligned with

the x-axis. The x-axis, y-axis, and z-axis are along the axial direction, lateral direction, and elevational direction, respectively.

A. Locally Affine Model for Tissue Motion

Both the coupled filtering method and the affine warping method use a locally affine model to approximate the tissue motion

$$\vec{p}_n' = M\vec{p}_n + \vec{T} \tag{1}$$

where $\vec{p}_n$, $\vec{p}_n'$ are the spatial positions of the nth tissue scatterer before and after the tissue motion (i.e., an element of tissues that scatters ultrasound waves). M and $\vec{T}$ denote motion parameters in the locally affine model. M is a 3×3 matrix describing the tissue deformation and rotation in the local area

$$M = \begin{bmatrix} M_{xx} & M_{xy} & M_{xz} \\ M_{yx} & M_{yy} & M_{yz} \\ M_{zx} & M_{zy} & M_{zz} \end{bmatrix} \tag{2}$$

and $\vec{T}$ is a 3×1 vector denoting the translation of tissue scatterers. Different types of tissue motion are modeled, including translation, compression, expansion, shearing, and rotation.

In traditional methods, tissue displacements are estimated. The strains and rotations of tissues are derived by taking partial derivatives of the tissue displacements. In the locally affine model, motion parameters M and $\vec{T}$ are estimated. Tissue displacements can be derived from the motion parameters

$$\vec{d}_n = \vec{p}_n' - \vec{p}_n = (M - I)\vec{p}_n + \vec{T} \tag{3}$$

where $\vec{d}_n$ is the displacement of the nth tissue scatterer and I is a 3×3 identity matrix. According to the infinitesimal strain theory [31], the strains and rotation angles are only combinations of the elements in the matrix M

$$\epsilon_{xx} = M_{xx} - 1$$
$$\epsilon_{yy} = M_{yy} - 1$$
$$\epsilon_{zz} = M_{zz} - 1$$
$$\epsilon_{yz} = \frac{(M_{yz} + M_{zy})}{2}$$
$$\epsilon_{zx} = \frac{(M_{zx} + M_{xz})}{2}$$
$$\epsilon_{xy} = \frac{(M_{xy} + M_{yx})}{2}$$
$$\theta_{yz} = \frac{(M_{zy} - M_{yz})}{2}$$
$$\theta_{zx} = \frac{(M_{xz} - M_{zx})}{2}$$
$$\theta_{xy} = \frac{(M_{yx} - M_{xy})}{2}.$$

Note that the unit of rotation angles θ is radian instead of degree. The strains do not have a unit.

B. Linear Convolution Model for Speckle Patterns

In the coupled filtering method, a linear convolution model is used to describe the speckle patterns formed by the interference of ultrasound waves reflected by tissue scatterers [32]–[34]

$$I(\vec{X}; P) = Z(\vec{X}; P) * H(\vec{X}). \tag{4}$$

The above equation states that, within a local area (i.e., in the full-width half-maximum of the PSF [35]), the speckle pattern $I(\vec{X}; P)$ can be described as a convolution between the tissue scatterers $Z(\vec{X}; P)$ and the point spread function (PSF) of the imaging system $H(\vec{X})$. Here $I(\vec{X}; P)$ denotes the speckle pattern formed by interference of backscattered ultrasound waves within the local area, $\vec{X}$ denotes the 3-D coordinates of the image volume, and P is the set of tissue scatterer parameters

$$P = \{(a_1, \vec{p}_1), (a_2, \vec{p}_2), \ldots, (a_N, \vec{p}_N)\} \tag{5}$$

where a_n denotes the reflectance coefficient of the nth tissue scatterer, showing how much ultrasound waves are reflected by the scatterer. $\vec{p}_n$ denotes the spatial position of the nth tissue scatterer, $n = 1, 2, \ldots, N$. N is the total number of tissue scatterers. In (4), the tissue scatterers are modeled as a summation of N 3-D Dirac functions

$$Z(\vec{X}; P) = \sum_{n=1}^{N} a_n \delta(\vec{X} - \vec{p}_n). \tag{6}$$

The equation above is based on the assumption that tissue scatterers have a small size with respect to the PSF wavelength [34], [36]. The PSF is dependent on the configuration of the ultrasound system (e.g., the shape and element arrangement of the transducer, the central frequency, and bandwidth of transmitted ultrasound waves, etc.), and generally does not have an explicit expression. In some literature [33], [34], the PSF is approximated as a Gaussian weighted cosine function

$$H(\vec{X}) = e^{-(1/2)\vec{X}^T \Gamma \vec{X}} \cos\left(2\pi \vec{X}^T \vec{U}_0\right) \tag{7}$$

where Γ is a 3×3 diagonal matrix with diagonal elements $1/\sigma_x^2$, $1/\sigma_y^2$ and $1/\sigma_z^2$, respectively, and $\vec{U}_0 = (u_x, 0, 0)^T$, denotes the spatial frequency of the transducer. Alternatively, the PSF can also be calculated by numerically solving acoustic wave equations with specified boundary conditions [37].

As a summary, the ultrasound images formed by the interference of backscattered ultrasound waves before and after the tissue motion read

$$I(\vec{X}; P) = Z(\vec{X}; P) * H(\vec{X})$$
$$= \sum_{n=1}^{N} a_n \delta(\vec{X} - \vec{p}_n) * H(\vec{X})$$
$$I(\vec{X}; P') = Z(\vec{X}; P') * H(\vec{X})$$
$$= \sum_{n=1}^{N} a_n \delta(\vec{X} - \vec{p}_n') * H(\vec{X})$$
$$\vec{p}_n' = M\vec{p}_n + \vec{T}$$

where P and P' denote the set of tissue scatterer parameters before and after tissue motion, respectively. In this paper, we assume that the two sets of tissue scatterers share the same reflectance coefficients [34], [36]

$$P = \{(a_1, \vec{p}_1), (a_2, \vec{p}_2), \ldots, (a_N, \vec{p}_N)\}$$
$$P' = \{(a_1, \vec{p}_1'), (a_2, \vec{p}_2'), \ldots, (a_N, \vec{p}_N')\}.$$

The goal of motion estimation is to reliably estimate motion parameters M and $\vec{T}$.

C. The Coupled Filtering Method

In the coupled filtering method [30], an affine warping procedure is proposed to compensate for the geometric transformation of speckle patterns. An affine transform is first applied to the image after the tissue motion so that tissue scatterers return to their original positions

$$I(M\vec{X} + \vec{T}; P') = Z(\vec{X}; P) * H(M\vec{X}) \qquad (8)$$

where parameters in the affine transform M and $\vec{T}$ are assumed to be the same as the underlying true motion parameters in (1). The proof of (8) is shown in (9) and (10). First consider the affine transform applied to the tissue scatterers $Z(\vec{X}; P')$ after the tissue motion

$$
\begin{aligned}
Z(M\vec{X} + \vec{T}; P') &= \sum_{n=1}^{N} a_n \delta(M\vec{X} + \vec{T} - \vec{p}'_n) \\
&= \sum_{n=1}^{N} a_n \delta(M\vec{X} + \vec{T} - M\vec{p}_n - \vec{T}) \\
&= \sum_{n=1}^{N} \frac{a_n}{|M|} \delta(\vec{X} - \vec{p}_n) \\
&= \frac{1}{|M|} Z(\vec{X}; P) \qquad (9)
\end{aligned}
$$

where $|M|$ denotes the determinant of the matrix M. The above equation shows that tissue scatterers return to their original positions if the affine warping procedure is applied to tissue scatterers with appropriate motion parameters. Then consider the affine warping procedure applied to the ultrasound image, which is a convolution of the tissue scatterers and the PSF

$$
\begin{aligned}
&I(M\vec{X} + \vec{T}; P') \\
&= \int_{R^3} Z(M\vec{X} + \vec{T} - \vec{X}'; P') H(\vec{X}') d\vec{X}' \\
&= \int_{R^3} Z\left(M(\vec{X} - M^{-1}\vec{X}') + \vec{T}; P'\right) H(\vec{X}') d\vec{X}' \\
&\stackrel{(\star)}{=} \int_{R^3} \frac{1}{|M|} Z\left(\vec{X} - M^{-1}\vec{X}'; P\right) H(\vec{X}') d\vec{X}' \\
&\stackrel{(\star\star)}{=} \int_{R^3} Z\left(\vec{X} - \vec{X}''; P\right) H(M\vec{X}'') d\vec{X}'' \\
&= Z(\vec{X}; P) * H(M\vec{X}) \qquad (10)
\end{aligned}
$$

where at the step with $(\star)$, (9) is used and at the step with $(\star\star)$, a substitution of the integral variable $\vec{X}'' = M^{-1}\vec{X}'$ is performed.

Comparing (4) with (8), one can find that the pair of ultrasound images share the same tissue scatterer term after the application of the affine warping procedure. The affine warping procedure is able to compensate for the geometric transformation of speckle patterns. The remaining difference between $I(\vec{X}; P)$ and $I(M\vec{X} + \vec{T}; P')$ lies in the PSF term, which implies that the

speckle pattern has been changed (e.g., a different interference of reflected ultrasound waves). Therefore, a pair of PSF related filters can be applied to $I(\vec{X}; P)$ and $I(M\vec{X} + \vec{T}; P')$, respectively

$$I(\vec{X}; P) * H(M\vec{X}) = Z(\vec{X}; P) * H(\vec{X}) * H(M\vec{X}) \qquad (11)$$

$$I(M\vec{X} + \vec{T}; P') * H(\vec{X}) = Z(\vec{X}; P) * H(M\vec{X}) * H(\vec{X}). \qquad (12)$$

The above filtering is called the coupled filtering procedure. It is easy to see that speckle patterns become identical to each other after applying the affine warping procedure and the coupled filtering procedure

$$I(M\vec{X} + \vec{T}; P') * H(\vec{X}) = I(\vec{X}; P) * H(M\vec{X}). \qquad (13)$$

Speckle pattern variations due to the locally affine tissue motion can be eliminated if the linear convolution model is valid in the local area.

Based on the insight above, a coupled filtering method is proposed [30], in which the estimation of motion parameters is achieved by searching for the optimal motion parameters that best satisfy (13). For example, the correlation coefficient between $I(M\vec{X} + \vec{T}; P') * H(\vec{X})$ and $I(\vec{X}; P) * H(M\vec{X})$ is maximized. Alternatively, the sum of absolute difference (SAD) or the sum of square difference (SSD) between the two images can be minimized. The coupled filtering method is able to achieve reliable estimation of tissue motion even when tissue deformation or rotation is very large [30].

D. The Affine Warping Method

Although the coupled filtering method has a good performance in reducing speckle pattern variations, it only works for RF images. In order to explain this limitation in detail, we would like to describe the relationship between an RF image and its corresponding BM image

$$
\begin{aligned}
I_{BM}(\vec{X}; P) &= \left| I(\vec{X}; P) + j\Phi\left\{I(\vec{X}; P)\right\} \right| \\
&= \Big| Z(\vec{X}; P) * H(\vec{X}) \\
&\quad + j\Phi\left\{Z(\vec{X}; P) * H(\vec{X})\right\} \Big| \qquad (14)
\end{aligned}
$$

where $I(\vec{X}; P)$ denotes the RF image and $I_{BM}(\vec{X}; P)$ denotes the corresponding BM image; j is the imaginary unit; Φ denotes the Hilbert transform along the beam direction; $|\cdot|$ denotes the absolute value of a complex number; $Z(\vec{X}; P)$ and $H(\vec{X})$ denote the tissue scatterers and the PSF of the system, respectively. If $Z(\vec{X}; P)$ is a summation of Dirac functions and $H(\vec{X})$ is a Gaussian weighted cosine function, the above equation can be further simplified as

$$\Phi\{Z(\vec{X}; P) * H(\vec{X})\} = Z(\vec{X}; P) * \Phi\{H(\vec{X})\}, \qquad (15)$$

$$I_{BM}(\vec{X}; P) = \left| Z(\vec{X}; P) * \left(H(\vec{X}) + j\Phi\{H(\vec{X})\}\right) \right| \qquad (16)$$

where $\Phi\{H(\vec{X})\}$ is a Gaussian weighted sine function corresponding to the $H(\vec{X})$ in (7). Note that (16) cannot be further

simplified as a single convolution. For instance, the following equation does not hold:

$$I_{BM}(\vec{X}; P) \neq Z(\vec{X}; P) * \left| \left(H(\vec{X}) + j\Phi\{H(\vec{X})\} \right) \right|. \quad (17)$$

Therefore, the equality relationship in (13) does not hold for BM images. As a consequence, the coupled filtering method is not applicable to BM images.

In order to compensate for the speckle pattern variations in BM images, we propose an affine warping method. As depicted in Fig. 1(b), the affine warping method only involves an affine warping procedure and compensates for the geometric transformation of speckle patterns. It does not compensate for the intensity change of speckle patterns appropriately since it only assumes a linear relationship between pixel intensities (e.g., if correlation coefficient is used as the metric). However, the affine warping method is computationally more efficient than the coupled filtering method. More importantly, the affine warping method can be applied to both BM and RF images. Instead of searching for optimal motion parameters that best satisfy (13), the affine warping method aims at finding optimal parameters that maximize the correlation or minimize the difference between $I(M\vec{X} + \vec{T}; P')$ and $I(\vec{X}; P)$. Here $I(\vec{X}; P)$ and $I(\vec{X}; P')$ are the images before and after the tissue motion, respectively. They can be either RF images or BM images. In Sections III–VII, we will show that in most cases, the affine warping method achieves a similar performance as the coupled filtering method.

E. Related Methods

1) The Direct Correlation Method: Fig. 1 depicts essential components of the coupled filtering method, the affine warping method and the direct correlation method. The coupled filtering method can be viewed as the direct correlation method with an affine warping procedure and a coupled filtering procedure, while the affine warping method can be viewed as the direct correlation method with the affine warping procedure only. They are related in different aspects.

- Compensation of speckle variations: The coupled filtering method compensates for both the geometric transformation and the intensity change of speckle patterns. Remaining variations include the variation in the PSFs at different spatial positions. The affine warping method only compensates for the geometric transformation of speckle patterns. The direct correlation method assumes that no feature motion decorrelation exists (e.g., speckle patterns are invariant during the tissue motion) and no compensation of speckle pattern variations is made.

- Underlying models and assumptions: The coupled filtering method assumes that a linear convolution model can be used to describe the formation of ultrasound images, and the tissue motion is locally affine. The affine warping method is based on the locally affine model without the linear convolution model. The direct correlation method assumes that speckle patterns are invariant during the tissue motion. The affine warping method and the direct correlation method can be applied to both RF and BM

images. The coupled filtering method is applicable to RF images only.

2) The Companding Method: The companding method [27] compensates for the local compression and expansion of speckle patterns, but it does not deal with the shearing or rotation of tissues. The variation compensation procedure used in the companding method is equivalent to the affine warping procedure with an additional constraint stating that M is diagonal

$$M = \begin{bmatrix} M_{xx} & 0 & 0 \\ 0 & M_{yy} & 0 \\ 0 & 0 & M_{zz} \end{bmatrix}. \quad (18)$$

In Section VI, we will show that the compensation of tissue shearing and rotation is necessary in a typical elastography study with different stiffness regions. When tissue deformation is large, the companding method cannot sufficiently reduce speckle pattern variations for reliable motion estimation.

3) The Deconvolution Filter: A deconvolution filter has been proposed to compensate for the intensity change of speckle patterns [38]. Such a method applies the deconvolution filter to ultrasound images after the temporal stretching in [25]. However, such a method only compensates for speckle pattern variations caused by 1-D tissue motion and in practice an approximate filter is used to limit the amplification of high frequency components.

4) The Lagrangian Speckle Estimator: A Lagrangian speckle motion estimator (LSME) has also been proposed [3], [39]. The LSME method is one of the first model-based methods to compensate for the geometric transformation and the intensity change of speckle patterns. The differences between the two methods are as follows.

- Instead of applying a pair of filters to two images, the LSME method uses only one Wiener filter. As the Wiener filter is an approximate filter to suppress the response of high frequency components, the strict equality relationship is not achieved as in (13). Besides, the LSME method always uses the filter, while in this paper we would like to investigate whether such filtering is necessary.

- Regarding the optimization strategy for the motion parameters, different implementations have been proposed for the LSME method [40]–[43]. The best algorithm uses an optical flow based method for the fast optimization [42], [43]. The coupled filtering method and the affine warping method use a coarse to fine strategy to exhaustively search motion parameters close to the global optimum.

III. IMPLEMENTATION

Now we would like to present the technical details of finding the optimal motion parameters M and T in the coupled filtering method and the affine warping method. In order to obtain the global optimum, an exhaustive search is used and the search of different motion parameters is performed simultaneously but not iteratively. A coarse to fine optimization strategy is adopted to accelerate the high dimensional search. A tissue incompressibility constraint is also imposed to reduce the dimension of the search space. The redundancy in the affine warping procedure and the coupled filtering procedure for overlapping correlation

---

Algorithm 1 Motion Estimation at Each Scale

Input:
$I(\vec{X}; P), I(\vec{X}; P')$: The pair of ultrasound images
$\mathcal{W}$: The set of correlation windows
M_{range}, T_{range} : Search ranges for M and T
M_{step}, T_{step} : Search steps for M and T
M_{intp}, T_{intp} : Interpolation results from optimal solutions
               at the previous scale

Initialization:
$\forall W \in \mathcal{W}$,
if $scale = 1$ **then**
   $\mathcal{M}(W) = \{M| - M_{range}/2 \preceq M - I_{3\times3} \preceq M_{range}/2\}$
   $\mathcal{T}(W) = \{T| - T_{range}/2 \preceq T \preceq T_{range}/2\}$
else
   $\mathcal{M}(W) = \{M| - M_{range}/2 \preceq M - M_{intp}(W) \preceq M_{range}/2\}$
   $\mathcal{T}(W) = \{T| - T_{range}/2 \preceq T - T_{intp}(W) \preceq T_{range}/2\}$
end if
$C_{opt}(W) \leftarrow -2, M_{opt}(W) \leftarrow I_{3\times3}, T_{opt}(W) \leftarrow \vec{0}$.

Main Loop:
for $W \in \mathcal{W}$ **do**
  for $M \in \mathcal{M}(W)$ **do**
    for $T \in \mathcal{T}(W)$ **do**
     if the coupled filtering method **then**
       $F_1(\vec{X}) \leftarrow I_{\vec{X} \in W}(\vec{X}; P) * H(M\vec{X})$
       $F_2(\vec{X}) \leftarrow I_{\vec{X} \in W}(M\vec{X} + T; P') * H(\vec{X})$
     else if the affine warping method **then**
       $F_1(\vec{X}) \leftarrow I_{\vec{X} \in W}(\vec{X}; P)$
       $F_2(\vec{X}) \leftarrow I_{\vec{X} \in W}(M\vec{X} + T; P')$
     else
       $F_1(\vec{X}) \leftarrow I_{\vec{X} \in W}(\vec{X}; P)$
       $F_2(\vec{X}) \leftarrow I_{\vec{X} \in W}(\vec{X} + T; P')$
     end if
     $C \leftarrow \sum(F_1 \cdot F_2)/\sqrt{\sum(F_1^2) \cdot \sum(F_2^2)}$
     if $C > C_{opt}(W)$ **then**
       $C_{opt}(W) \leftarrow C, M_{opt}(W) \leftarrow M, T_{opt}(W) \leftarrow T$
     end if
    end for
  end for
end for

Output:
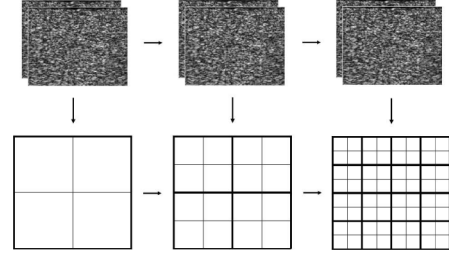**return** $C_{opt}, M_{opt}, T_{opt}$

Fig. 2. Coarse-to-fine strategy for motion estimation. Multiple scales are involved. At each scale, centers of correlation windows form a square lattice. The distance between neighboring correlation windows is reduced by half at each scale, and the number of correlation windows along each direction is doubled correspondingly. Only a few correlation windows far away from each other are used at the coarsest scale while windows highly overlapping with each other are used at the finest scale. The size of correlation windows is the same at all scales. The search range of motion parameters is reduced by half at each scale, while the search step is the same at all scales.

windows is minimized. Finally, the search algorithm is implemented with GPU based parallel computing.

A. A Coarse to Fine Strategy

In this paper, a coarse to fine strategy is used to accelerate the search of motion parameters in the coupled filtering method, the affine warping method and the direct correlation method. Multiple scales are used in the search. At each scale, centers of different correlation windows form a square lattice (Fig. 2). We use $\mathcal{W}$ to denote the set of all correlation windows. At the coarsest scale, only a few correlation windows far away from each other are used. A discrete search with sufficiently large search ranges $M_{\text{range}}, T_{\text{range}}$ and sufficiently small search steps $M_{\text{step}}, T_{\text{step}}$ is performed. Then at the finer scale, the distance between neighboring windows is reduced by half and the number of windows is doubled along each direction. The estimation results $M_{\text{opt}}, T_{\text{opt}}$ at the coarser scale are linearly interpolated to the finer scale. At the finer scale, the search of motion parameters is performed in the neighborhood of interpolation results $M_{\text{intp}}, T_{\text{intp}}$. The search ranges $M_{\text{range}}, T_{\text{range}}$ are reduced by half for each motion parameter, while the search

steps $M_{\text{step}}, T_{\text{step}}$ are the same at all scales. The interpolation of estimation results and the refinement of motion estimation are repeated until centers of neighboring windows have a minimal distance (e.g., one pixel). The search strategy at each scale has been depicted in Algorithm 1, where $\mathcal{W}$ is the set of correlation windows at a certain scale, $\mathcal{M}(W)$ and $\mathcal{T}(W)$ are the sets of all possible motion parameters Ms and Ts for a given correlation window W, $I_{3\times3}$ is a 3×3 identity matrix, $I_{\vec{X} \in W}(\vec{X}; P)$ is the local correlation window W of the input image $I(\vec{X}; P)$, $F_1(\vec{X})$ and $F_2(\vec{X})$ are the corresponding correlation windows for the two input images after the compensation procedures, and $\vec{0}$ is a vector with all zero elements. The generalized inequality operator $\preceq$ denotes that each element of the left-hand side is smaller than or equal to the corresponding element of the right-hand side.

In this paper, the correlation coefficient is used as the metric for the three methods. Correlation windows of the same size are used at all scales. A correlation window with a size between two to four times of the PSF size is used, so that the correlation window is large enough to contain features for tracking and at the same time not too large to make the assumption of affine tissue motion invalid. At all scales, no smoothing or down-sampling is performed on the pair of ultrasound images.

B. Constraints on Motion Parameters

Different constraints can be imposed on motion parameters to reduce the dimension of the search space. For example, a tissue incompressibility constraint [24] can be used, which states that the volume of tissues does not change under mechanical forces. In continuum mechanics [31], it is equivalent to the statement that the determinant of M is 1

$$|M| = 1. \tag{19}$$

Furthermore, suppose

$$M = \begin{bmatrix} 1 + \epsilon_{xx} & \epsilon_{xy} \\ \epsilon_{yx} & 1 + \epsilon_{yy} \end{bmatrix} \tag{20}$$

where $\epsilon_{xx}, \epsilon_{yy}$ are the axial strain and the lateral strain, and $\epsilon_{xy}, \epsilon_{yx}$ are the axial shear and the lateral shear, respectively. The following equation is satisfied:

$$(1 + \epsilon_{xx}) \times (1 + \epsilon_{yy}) - \epsilon_{xy} \times \epsilon_{yx} = 1. \tag{21}$$

When the strains are infinitesimal, the above equation is reduced to

$$\epsilon_{xx} + \epsilon_{yy} = 0. \qquad (22)$$

The tissue incompressibility constraint is generally true. Therefore, in 2-D images one only needs to search for ϵ_{xx}, ϵ_{xy}, and ϵ_{yx} independently for the optimization of the M matrix, while ϵ_{yy} is constrained to be the negative of ϵ_{xx}. Note that in the above equations, the axial shear ϵ_{xy} and the lateral shear ϵ_{yx} are the elements of the M matrix, and the shearing and rotation can be calculated by

$$s_{xy} = \frac{(\epsilon_{xy} + \epsilon_{yx})}{2} \qquad (23)$$

$$\theta_{xy} = \frac{(\epsilon_{yx} - \epsilon_{xy})}{2}. \qquad (24)$$

For 3-D speckle tracking, a similar conclusion can be drawn

$$\epsilon_{xx} + \epsilon_{yy} + \epsilon_{zz} = 0. \qquad (25)$$

Therefore, one does not need to search for ϵ_{zz} independently as ϵ_{xx} and ϵ_{yy}. ϵ_{zz} is constrained to be the negative of $\epsilon_{xx} + \epsilon_{yy}$. Such a tissue incompressibility constraint is able to reduce the M search space by 1.

C. Redundancy in Compensation Procedures

In Algorithm 1, the affine warping procedure and the coupled filtering procedure for the compensation of speckle pattern variations are conducted separately for each correlation window. For highly overlapping correlation windows at the finer scales, such local compensation procedures are performed repeatedly. To eliminate such a redundancy, the affine warping procedure and the coupled filtering procedure are applied globally to the whole ultrasound image. Then different correlation windows are selected for the calculation of correlation coefficients and the search of motion parameters. The main loop of the updated algorithm is shown in Algorithm 2. $I'(\vec{X})$ and $I''(\vec{X})$ are the two input images after the global compensation procedures. $F_1(\vec{X})$ and $F_2(\vec{X})$ are the corresponding correlation windows in $I'(\vec{X})$ and $I''(\vec{X})$.

D. Parallel Computation

Graphics processing unit (GPU) based parallel computation is used to accelerate the search of motion parameters. Given a pair of ultrasound images after the compensation of speckle pattern variations, correlation coefficients between different pairs of correlation windows are calculated in parallel. The affine transformation of the ultrasound images and the convolution between the ultrasound images and the PSF related filters are also performed in parallel.

IV. STUDY ON DIFFERENT SPECKLE PATTERN VARIATIONS

In this section, we aim to study the effects of the two types of speckle pattern variations on motion estimation. A comparative study of the coupled filtering method, the affine warping method

---

Algorithm 2 Main Loop for the Updated Algorithm

> **for** $M \in \mathcal{M}(W)$ **do**
>   **for** $T \in \mathcal{M}(W)$ **do**
>   **if** the coupled filtering method **then**
> $I'(\vec{X}) \leftarrow I(\vec{X}; P) * H(M\vec{X})$
> $I''(\vec{X}) \leftarrow I(M\vec{X} + T; P') * H(\vec{X})$
>   **else if** the affine warping method **then**
> $I'(\vec{X}) \leftarrow I(\vec{X}; P)$
> $I''(\vec{X}) \leftarrow I(M\vec{X} + T; P')$
>   **else**
> $I'(\vec{X}) \leftarrow I(\vec{X}; P)$
> $I''(\vec{X}) \leftarrow I(\vec{X} + T; P')$
>   **end if**
>   **for** $W \in \mathcal{W}$ **do**
> $F_1(\vec{X}) \leftarrow I'_{\vec{X} \in W}(\vec{X})$
> $F_2(\vec{X}) \leftarrow I''_{\vec{X} \in W}(\vec{X})$
> $C \leftarrow \sum(F_1 \cdot F_2)/\sqrt{\sum(F_1^2) \cdot \sum(F_2^2)}$
>   **if** $C > C_{opt}(W)$ **then**
> $C_{opt}(W) \leftarrow C, M_{opt}(W) \leftarrow M, T_{opt}(W) \leftarrow T$
>   **end if**
>   **end for**
>   **end for**
> **end for**

---

and the direct correlation method is conducted. The validity of (13) is examined and the effects of different types of speckle pattern variations are studied. Both 2-D/3-D simulation and 2-D phantom experiment are conducted in the comparative study.

A. 2-D Simulation Results

In 2-D simulation, we aim to examine the performance of the coupled filtering method, the affine warping method and the direct correlation method in typical elastography studies. Tissues are simulated within a region of 50 mm $\times$ 40 mm $\times$ 10 mm that lies at the depth between 50 and 100 mm. In order to mimic the behavior of the cancerous tissue, an eclipse shaped tissue region with a higher stiffness is inserted at the center of the ROI. The diameter of the stiffer region is 20 and 16 mm along the axial direction and the lateral direction, respectively, and the stiffness ratio between the two different regions is 4. In the 2-D simulation, the upper surface of the tissues (e.g., the 40 mm $\times$ 10 mm surface at the depth of 50 mm) is uniformly compressed downwards by 5%. The ultrasound imaging transducer is always 50 mm above from the upper surface and therefore the equivalent tissue motion is the compression upwards from the bottom surface. The tissue motion along the elevational direction is assumed to be 0 (i.e., the tissue region is not allowed to move along the elevational direction), and the tissue motion along the axial and lateral directions is calculated via the finite element analysis powered by the Ansys Structural Mechanics Solutions. The boundary conditions are set such that the upper surface is fixed as well as the two side surfaces parallel to the axial–lateral plane, while other side surfaces are free to move. The simulated tissue motion is shown in Fig. 3. The dominant motion is the axial compression and the lateral expansion. With the stiffer region in the center, the softer region above tends to be compressed more than the softer region laterally away from the center. Therefore a higher normal strain exists for the softer region above the stiffer region. Shearing as well as rotation are observed at the four corners around the stiffer region.
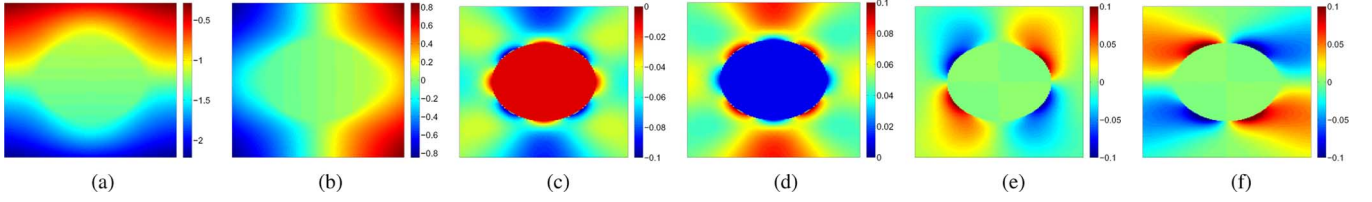
Fig. 3. Simulated 2-D tissue motion and deformation. A stiffer region is designed at the center of the ROI. Tissues are compressed downwards by 5 percent. (a) Axial displacements. (b) Lateral displacements. (c) Axial strains. (d) Lateral strains. (e) Axial shears. (f) Lateral shears.

In 2-D simulation, a linear convolution model based toolbox known as the Field II program [37], [44], [45] is used to generate simulated ultrasound images through a convolution of random tissue scatterers and the PSF of the imaging system. A total of 1 000 000 tissue scatterers are randomly distributed in the 50 mm × 40 mm × 10 mm tissue region, and the reflectance coefficients follow a Gaussian distribution bounded between 0 and 1. The PSF of the imaging system is calculated by solving the acoustic wave equations. A linear array of 64 transducer elements is selected as the ultrasound transducer. The central frequency of transducer is 3 MHz and the fractional bandwidth is 0.5. The bandwidth is defined as the full-width at half-maximum (FWHM) of transmitted waves. Dynamic focusing is used to reduce the variation in PSFs at different spatial positions, achieving a high resolution at different depths. The FWHM of the PSF is about 0.6 mm × 1.6 mm × 1.6 mm. On average there are approximately 400 tissue scatterers in each PSF. Although tissue scatterers are randomly distributed in a 3-D region, only a 2-D intersection parallel to the axial-lateral plane is extracted for 2-D ultrasound images. The generated 2-D images are based on the interference of echoes from all tissues scatterers near the intersection plane. In 2-D images, the spatial sampling frequencies along the axial direction and the lateral direction are 20 pixels/mm and 5 pixels/mm, respectively. The size of the 2-D image is 1001×201 pixels.

In the coupled filtering method and the affine warping method, only one tissue incompressibility constraint [24] is applied. Correlation coefficient is used as the metric instead of SAD and SSD since it provides a normalized measure showing how much speckle pattern variations have been eliminated. For example, a correlation coefficient of 1 implies a perfect match between the two images and a full compensation of speckle pattern variations. At the coarsest scale, the search ranges for M and T are

$$M_{\text{range}} = \begin{bmatrix} 20\% & 10\% \\ 10\% & 20\% \end{bmatrix}$$

$$T_{\text{range}} = 0.03 \times \begin{bmatrix} 1000 \\ 200 \end{bmatrix}$$

in which T_{range} has a unit of pixels and is set as 3% of the input image size. The search steps for M and T are:

$$M_{\text{step}} = \begin{bmatrix} 0.2\% & 0.2\% \\ 0.2\% & 0.2\% \end{bmatrix}$$

$$T_{\text{step}} = \begin{bmatrix} 1 \\ 1 \end{bmatrix}$$

in which each element represents the search step for the corresponding motion parameter. At the finest scale, $193 \times 129 =$

24897 windows are used for each 2-D image. The size of the correlation window is three times the PSF size (i.e., 37×25 pixels) at all scales. The performances of the coupled filtering method, the affine warping method and the direct correlation method are depicted in Fig. 4. In the coupled filtering method and the affine warping method, strains are deduced directly from the optimal motion parameter M. In the direct correlation method, where only translation is assumed in the local area and M is equal to the identity matrix I, strains are inferred by differentiating the axial and lateral displacements.

As depicted in Fig. 3, in the 2-D simulation the tissue strain can be as large as 10%. Boundaries between different stiffness regions are also present with a high contrast of strains, which may lead to the assumption of the locally affine tissue motion to be violated. The coupled filtering method and the affine warping method are able to provide reliable normal strain estimations. The stiffer region with a lower strain is revealed and a higher strain is also detected right above and below the stiffer region. The axial shears are revealed with some failures at the four corners around the stiffer region, mainly because the sharp change of tissue strains in those regions makes the assumption of locally affine motion invalid. The lateral shears cannot be estimated accurately, mainly because the sampling rate along the lateral direction is too low to provide enough information for the deformation estimation. The lateral strains are estimated robustly since they are constrained to be the opposite of the axial strains. Correlation coefficients for the two methods drop at the four corners around the stiffer region. For the direct correlation method, reasonable strain estimations cannot be provided and the correlation coefficients outside the stiffer region are lower than 0.5.

Since the true tissue strains are known in 2-D simulation, the performances of the three methods can be evaluated quantitatively. Suppose the true tissue strain for a certain correlation window W is $\epsilon_0(W)$. For the estimated strain $\epsilon(W)$ in different correlation windows, the square root of the mean square errors (SRMSE) is defined as

$$\text{SRMSE} = \sqrt{\frac{\sum_W (\epsilon(W) - \epsilon_0(W))^2}{N_W}} \tag{26}$$

where N_W denotes the number of correlation windows. In this simulation, the SRMSEs for the strain estimations are depicted in Table I. The performance of the affine warping method is similar to that of the coupled filtering method. For the axial/lateral strain estimation and the axial shear estimation, the estimation errors are less than 3%. For the lateral shear estimation, the estimation error is comparable to the estimated strain because of the
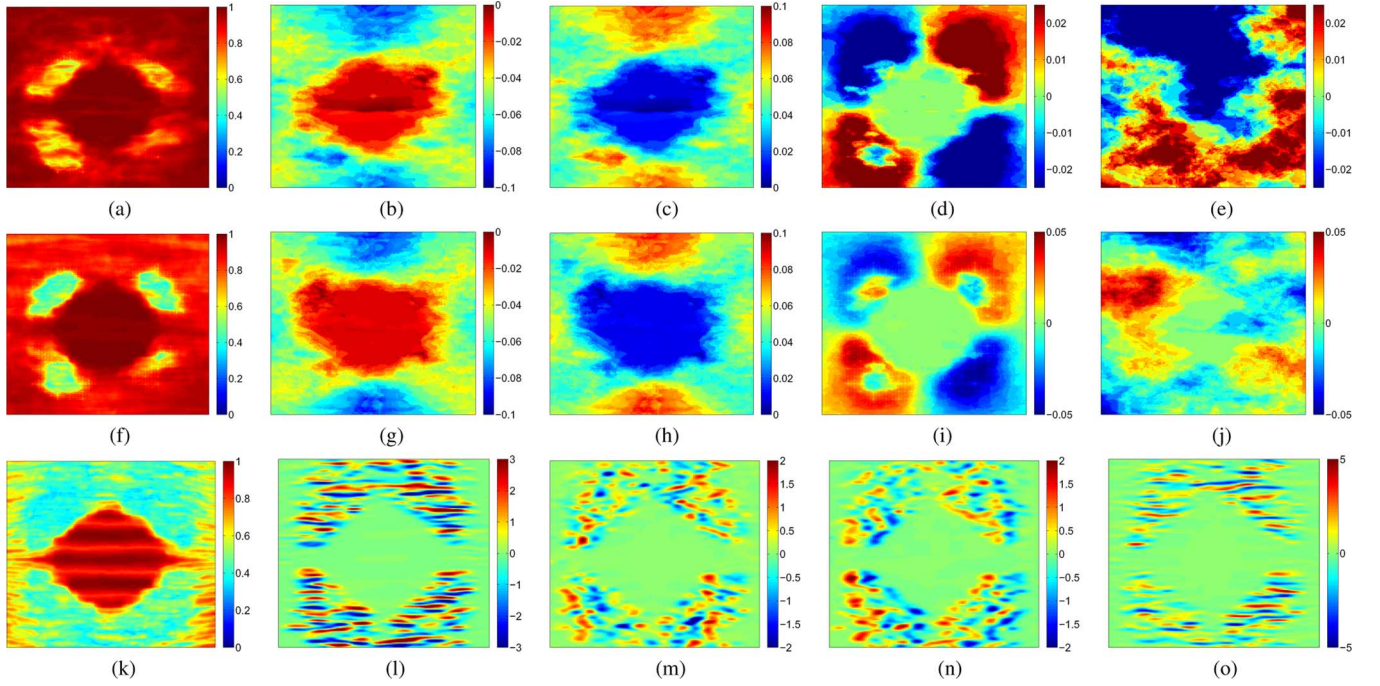
Fig. 4. 2-D simulation results. A stiffer region is designed at the center of the ROI. The tissue incompressibility constraint is applied. Row 1: The coupled filtering method. Row 2: The affine warping method. Row 3: The direct correlation method. Column 1: Correlation coefficients. Column 2: Axial strains. Column 3: Lateral strains. Column 4: Axial shears. Column 5: Lateral shears.

TABLE I
SRMSEs OF STRAIN ESTIMATIONS

	ϵ_{xx}	ϵ_{xy}	ϵ_{yx}	ϵ_{yy}
The Coupled Filtering Method	2.68%	2.28%	5.07%	2.68%
The Affine Warping Method	2.82%	2.22%	3.80%	2.82%
The Direct Correlation Method	94.15%	43.9%	92.23%	40.71%

low sampling rate along the lateral direction. The direct correlation method has a much higher estimation error than the coupled filtering method and the affine warping method.

B. 2-D Phantom Results

In 2-D phantom experiment, an elastography study with a soft, tissue-mimicking gelatin phantom is conducted [15]. A stiff cylindrical region is included at the center and a thin channel filled with fluids is also inside the phantom. The stiff region is about six times stiffer than the soft gelatin region. The stiff cylindrical region is designed to represent a breast lesion while the thin channel is designed to mimic a blood vessel. The top surface of the phantom is compressed down uniformly by 5% by the transducer surface. Ultrasound images before and after the compression are recorded. During the imaging, the bottom of the phantom is fixed while two of the side surfaces are restricted to prevent the out-of-plane motion of tissues. The central frequency of transducer is 7.2 MHz and the bandwidth is about 4.5 MHz. Equivalently, the spatial frequency is 9.35 cycles/mm and the spatial resolution along the beam direction is 0.15 mm. A Gabor function with the same spatial frequency and bandwidth is used to approximate the PSF of the ultrasound system. The lateral resolution is twice as coarse as the axial resolution. The spatial sampling rates are 74 pixels/mm and

5 pixels/mm, respectively. The phantom image produced has 3000×312 pixels.

In the phantom experiment, the parameter setting is the same as in the 2-D simulation. The performances of the coupled filtering method, the affine warping method and the direct correlation method are depicted in Fig. 5. Although only a qualitative analysis is available in the phantom experiment because of the unknown true tissue displacements, similar conclusions can be drawn as in the 2-D simulation.

As a benchmark in the comparison, the direct correlation method fails to produce reliable estimations. The correlation coefficients in the soft gelatin region decrease dramatically. On contrast, the correlation coefficients are above 0.9 in the stiff cylindrical region, mainly because tissue deformation or rotation is small in the region and little speckle pattern variations are present. The coupled filtering method and the affine warping method are able to robustly estimate the axial displacement related strains, but fail to reveal the lateral displacement related strains. The lateral strains can be estimated because of the tissue incompressibility constraint. Both methods are able to reveal the stiff cylindrical region with lower strains and the channel region with higher strains. Reasonable strain estimations can be produced except at some boundaries between two or more different regions, where multiple tissue motions exist. Although the thin fluid-filled channel is revealed for both methods, the boundary is not characterized clearly enough. At the corners where three different regions meet, a wrong estimation of the strains can be observed. Both the coupled filtering method and the affine warping method produce reasonable correlation coefficients except at the boundary regions, where a significant drop can be observed. The high correlation coefficients show that both methods are able to compensate for most of speckle
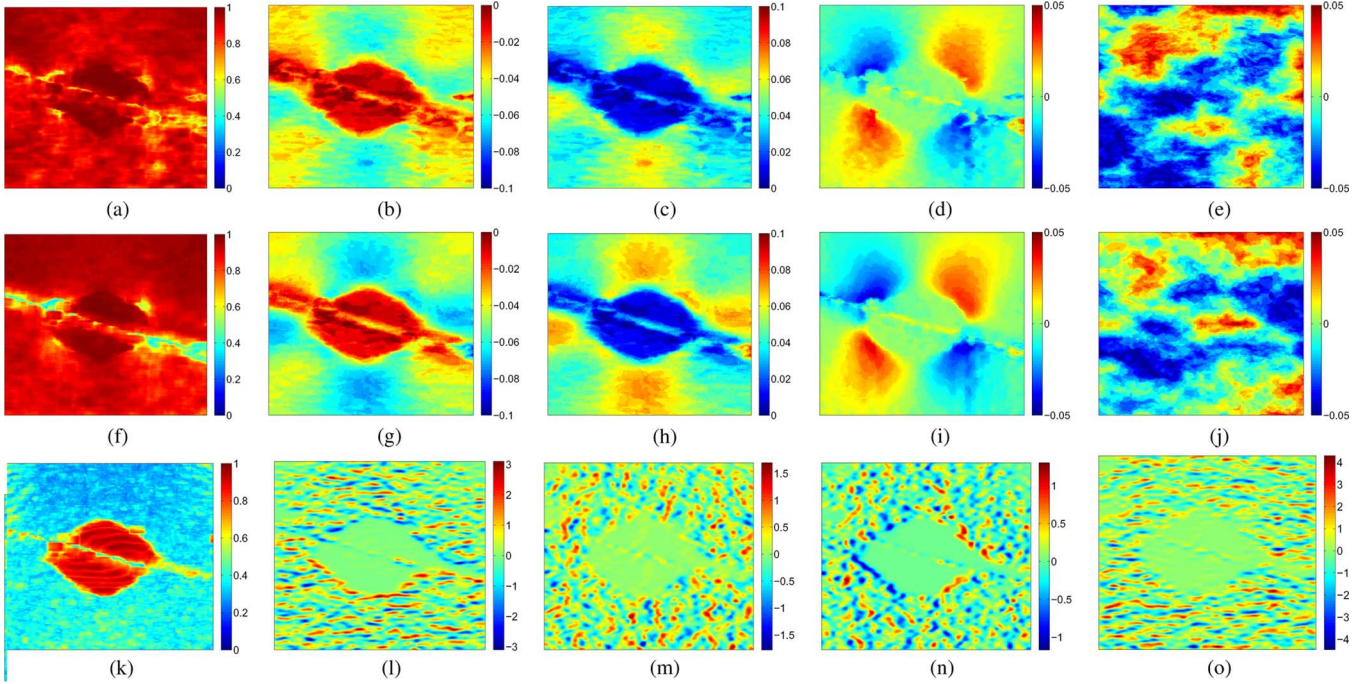
Fig. 5. 2-D phantom experiment results. A stiff cylindrical region is included and a fluid-filled thin channel is present in the phantom. The tissue incompressibility constraint is applied. Row 1: The coupled filtering method. Row 2: The affine warping method. Row 3: The direct correlation method. Column 1: Correlation coefficients. Column 2: Axial strains. Column 3: Lateral strains. Column 4: Axial shears. Column 5: Lateral shears.

pattern variations, and a similar performance of both methods implies that the compensation of the geometric transformation of speckle patterns is sufficient for motion estimation.

C. 3-D Simulation Results

In 3-D simulation, we mainly examine the validity of (13). We simulate 3-D ultrasound volumes under different kinds of tissue motion. For each tissue motion, we search for the optimal motion parameter and we use true values for other motion parameters to compensate for the speckle pattern variations. Six cases of tissue motion are simulated. In each case, only one type of motion is modeled. The M matrix in (1) for the six cases are shown as below

$$M = \begin{bmatrix} 1-\epsilon & 0 & 0 \\ 0 & 1+0.5\epsilon & 0 \\ 0 & 0 & 1+0.5\epsilon \end{bmatrix} \qquad (27)$$

$$M = \begin{bmatrix} 1+0.5\epsilon & 0 & 0 \\ 0 & 1-\epsilon & 0 \\ 0 & 0 & 1+0.5\epsilon \end{bmatrix} \qquad (28)$$

$$M = \begin{bmatrix} 1 & 0 & 0 \\ 0 & 1 & \epsilon \\ 0 & \epsilon & 1 \end{bmatrix} \qquad (29)$$

$$M = \begin{bmatrix} 1 & \epsilon & 0 \\ \epsilon & 1 & 0 \\ 0 & 0 & 1 \end{bmatrix} \qquad (30)$$

$$M = \begin{bmatrix} 1 & 0 & 0 \\ 0 & 1 & -\theta \\ 0 & \theta & 1 \end{bmatrix} \qquad (31)$$

$$M = \begin{bmatrix} 1 & 0 & \theta \\ 0 & 1 & 0 \\ -\theta & 0 & 1 \end{bmatrix}. \qquad (32)$$

They represent the axial compression/expansion (i.e., compression/expansion primarily along the axial direction), lateral compression/expansion (i.e., compression/expansion primarily along the lateral direction), shearing along the lateral-elevational plane (i.e., the elastic axis is aligned to the beam direction), shearing along the axial-lateral plane (i.e., the elastic axis is perpendicular to the beam direction), axial rotation (i.e., the rotation axis is aligned to the beam direction), and lateral rotation (i.e., the rotation axis is perpendicular to the beam direction), respectively. Normal strains ϵ in (27) and (28) vary from -20% to 20% at a step of 1%. Shear strains ϵ in (29) and (30) vary from -10% to 10% at a step of 1%. Rotation angles θ in (31) and (32) vary from -0.1 rad to 0.1 rad at a step of 0.01 rad. In the 3-D simulation, the translation vector $\vec{T}$ is set to be $\vec{0}$, assuming that the origin locates at the center of the ROI.

In order to generate ultrasound images from random tissue scatterers, the Field II program is used. A multi-row array transducer of 16×16 elements is used. The central frequency of the transducer is 3 MHz and the fractional bandwidth is 0.5. Dynamic focusing is used to reduce the variation in PSFs at different spatial positions. The 3-D PSF size (i.e., the FWHM of the PSF) is approximately 0.6 mm $\times$ 1.8 mm $\times$ 1.8 mm. A region of 10 mm $\times$ 10 mm $\times$ 10 mm is selected as the region of interest (ROI), which lies at the depth between 70 and 80 mm. A total of 2000 tissue scatterers are used in the 3-D simulation with the spatial positions following a uniform distribution in the ROI and the reflectance coefficients following a Gaussian distribution bounded between 0 and 1. In the region of each PSF, on average four tissue scatterers are present. The spatial sampling frequencies along the axial direction, the lateral direction and the elevational direction are 20 pixels/mm, 10 pixels/mm and 10 pixels/mm, respectively. The size of the 3-D image volume is $201 \times 101 \times 101$ voxels.
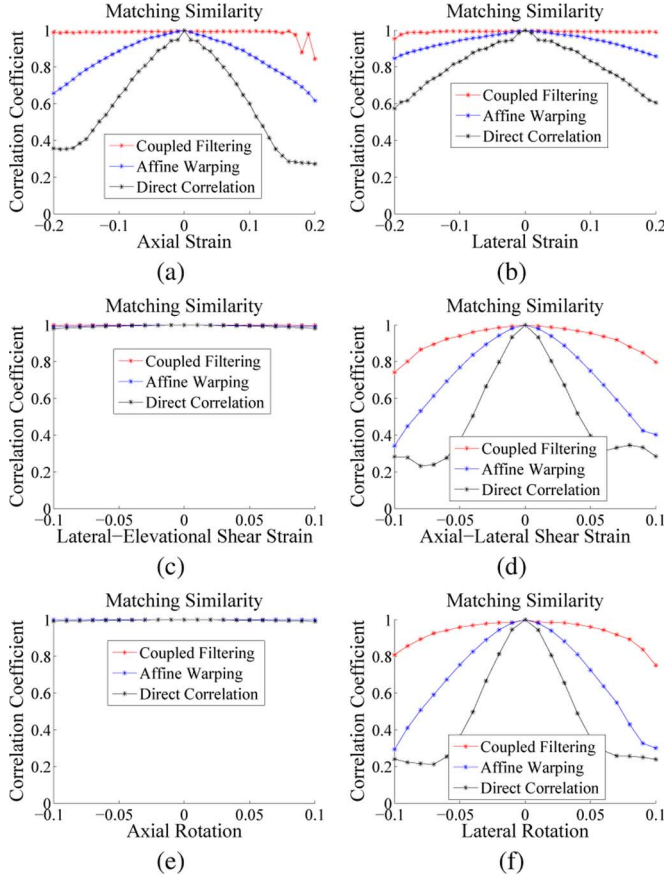
Fig. 6. Mean correlation coefficients under different types of 3-D tissue motion. The true tissue motion is used in the compensation of speckle pattern variations. (a) Axial compression/expansion. (b) Lateral compression/expansion. (c) Shearing along lateral–elevational plane. (d) Shearing along axial-lateral plane. (e) Axial rotation. (f) Lateral rotation.

Correlation coefficient is used as the metric in 3-D simulation. A correlation window with the size of 2 times as the PSF size is chosen (i.e., $25 \times 37 \times 37$ voxels). In total, $9 \times 9 \times 9 = 729$ correlation windows are used in each case. The mean correlation coefficients for the three methods are depicted in Fig. 6. The coupled filtering method is able to achieve a mean correlation coefficient close to 1 in most cases, showing that it is able to compensate for almost all speckle pattern variations. Exceptions include the case of shearing along the axial-lateral plane and the case of lateral rotation, where the mean correlation coefficients for the coupled filtering method start to drop when the applied strain or the rotation angle increases. This implies that (13) may not be true in these two cases. Speckle pattern variations other than the geometric transformation and the intensity change of speckle patterns are not neglectable (e.g., the variations of PSFs at different spatial positions). For the affine warping method, the mean correlation coefficients gradually drop as the applied strain or the rotation angle increases. However, they are remarkably higher than the mean correlation coefficients for the direct correlation method, especially when the applied strain or the rotation angle is large. It can be observed that both the geometric transformation and the intensity change of speckle patterns contribute to speckle pattern variations under large deformation or rotation. However, in the case of shearing along the

lateral–elevational plane and the case of axial rotation, speckle pattern variations are little. No axial motion exists and only smooth image patterns are available on the lateral–elevational plane, which have much lower frequency components than the RF signal along the axial direction. Therefore, in this case correlation coefficients decrease much less when speckle patterns do not match appropriately. Even the direct correlation method can achieve mean correlation coefficients above 0.98 with extremely large applied strains or rotation angles.

V. SPECKLE PATTERN VARIATIONS IN BM IMAGES

In this section, we study feature motion decorrelation in BM ultrasound images. Since the coupled filtering method is only applicable to RF images, we just compare the affine warping method with the direct correlation method.

A. 2-D Simulation Results

In this comparative study, the 2-D simulation is conducted with the same settings as in Section IV-A. The Field II program is used to generate the RF ultrasound images, which are then converted to BM images based on (14).

Fig. 7 shows that the affine warping method is able to reveal axial strains, axial shears and lateral strains robustly. However, it produces noisy strain images. The stiffness region is not characterized accurately. Besides, it fails to produce reasonable estimations of lateral shears as in RF images (Section IV-A). The direct correlation method cannot estimate strains correctly. Both the affine warping method and the direct correlation method are able to achieve correlation coefficients close to 1 in the boundaries between different regions of stiffness.

Table II shows that the estimation errors for the affine warping method are between 2% to 4%. The estimation errors for the direct correlation method are from 3% to 7%, which are as large as the estimated strains.

B. 2-D Phantom Results

2-D phantom experiment is also conducted with the BM images corresponding to the RF images in Section IV-B. Fig. 8 shows similar conclusions.

For BM images, both methods are able to achieve mean correlation coefficients close to 1. The affine warping method provides reasonable images for the axial strains, the lateral strains and the axial shears. However, the lateral shears cannot be estimated correctly. The direct correlation method is able to reveal axial strains and shear strains in the stiff region and in part of the soft region. The performance of the direct correlation method is enhanced in BM images, because feature motion decorrelation is reduced in BM images. The failure in the lower part of the soft region is due to a higher strain experienced (as indicated in the results of the affine warping method).

VI. EVALUATION OF SIMPLIFIED MOTION MODELS

This section tests the limit of simplified motion models. In particular, a tissue motion model only allowing 2-D translation, compression and expansion (i.e., restricting the motion parameter M to be diagonal as in the companding method [27]) is evaluated using the coupled filtering method and the affine warping
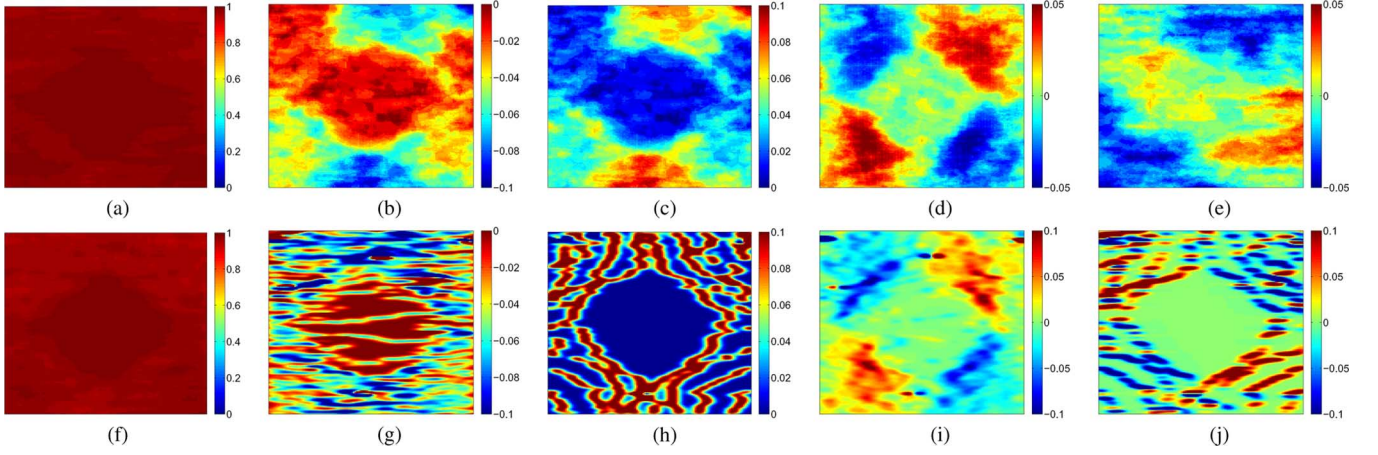
Fig. 7. 2-D simulation results, in which the affine warping method and the direct correlation method are applied to BM images. A stiffer region is designed at the center of the ROI. Row 1: The affine warping method. Row 2: The direct correlation method. Column 1: Correlation coefficients. Column 2: Axial strains. Column 3: Lateral strains. Column 4: Axial shears. Column 5: Lateral shears.
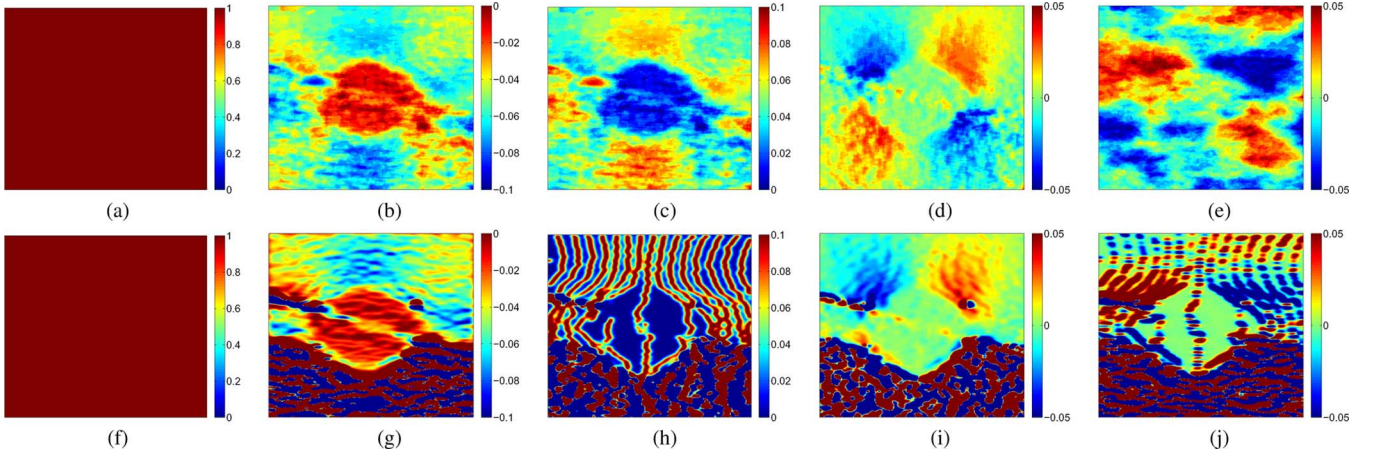

Fig. 8. 2-D phantom experiment results for the case of 5 percent compression, in which the affine warping method and the direct correlation method are applied to BM images instead of RF images. A stiff cylindrical region is included and a fluid-filled thin channel is present in the phantom. The tissue incompressibility constraint is applied. Row 1: The affine warping method. Row 2: The direct correlation method. Column 1: Correlation coefficients. Column 2: Axial strains. Column 3: Lateral strains. Column 4: Axial shears. Column 5: Lateral shears.

TABLE II
SRMSEs OF STRAIN ESTIMATIONS

	ϵ_{xx}	ϵ_{xy}	ϵ_{yx}	ϵ_{yy}
The Affine Warping Method	3.14%	2.36%	4.16%	3.14%
The Direct Correlation Method	4.48%	3.79%	6.9%	4.72%

method. The tissue incompressibility constraint is also used in this experiment.

Evaluation results are shown in Fig. 9. Mean correlation coefficients drop dramatically at the four corners. Normal strains are not estimated correctly. Thus, shearing and rotation shouldn't be ignored when speckle pattern variations are large. In general, a tissue motion model with shearing and rotation is necessary in a typical elastography study.

VII. Discussion

In this paper, we studied feature motion decorrelation under different conditions. We focused on two types of speckle pattern variations, the geometric transformation and the intensity
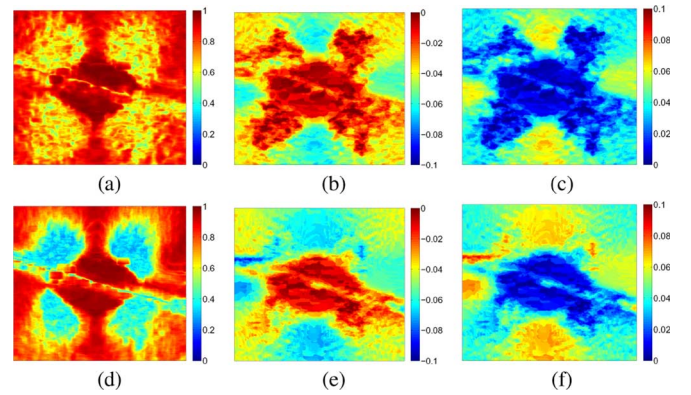

Fig. 9. 2-D phantom experiment results. A stiff cylindrical region is included and a fluid-filled thin channel is present in the phantom. Only translation, compression and expansion are allowed in the motion model. Row 1: The coupled filtering method. Row 2: The affine warping method. Column 1: Correlation coefficients. Column 2: Axial strains. Column 3: Lateral strains.

change of speckle patterns. Theoretical derivations and experimental results showed that the coupled filtering method is able

to compensate for both types of variations. The affine warping method is only able to compensate for the geometric transformation of speckle patterns. Nevertheless, both methods are able to achieve robust motion estimation. We do not consider speckle pattern variations caused by the out of plane motion since both methods can work in 3-D ultrasound images. In BM images, the affine warping method is generally able to estimate axial strains, lateral strains and axial shears correctly as in RF images. The direct correlation method fails when tissue motion and deformation is large. In this paper, we showed that a locally affine motion model is sufficient to approximate the tissue motion. A tissue motion model with only local translation, compression and expansion as in the companding method may be insufficient.

In this paper, simulations are conducted without random noises. A detailed study on the performances of the coupled filtering method and the affine warping method under different levels of random noises will also be interesting.

In clinical applications, the instrument dependent PSF needs to be identified for the coupled filtering method. As in the 2-D phantom experiment, a Gabor function can be used to approximate the real PSF. The central frequency and the bandwidth of the Gabor function can be decided from the transducer frequency and the transducer bandwidth. On the other hand, the affine warping method provides a similar performance and does not require knowledge of the PSF.

In this paper, two NVIDIA graphic cards (GeForce GTX 580) are used for the parallel computation. The program takes about 45 min for 2-D ultrasound images and is more than 60 times faster than the CPU-based program in a standard PC. Although the coupled filtering method and the affine warping method are able to handle extremely large feature motion decorrelation, they need a lot of computational time. A simultaneous search of motion parameters for 3-D ultrasound images is computationally inhibitory. For clinical applications, a fast algorithm is desired. We plan to further speed up the computation in our future work.

ACKNOWLEDGMENT

REFERENCES

[1] G. Trahey, J. Allison, and O. v. Ramm, "Angle independent ultrasonic detection of blood flow," *IEEE Trans. Biomed. Eng.*, vol. 34, no. 12, pp. 965–967, Dec. 1987.

[2] J. Ophir, S. K. Alam, B. Garra, F. Kallel, E. Konofagou, T. Krouskop, and T. Varghese, "Elastography: Ultrasonic estimation and imaging of the elastic properties of tissues," *J. Eng. Med.*, vol. 213, no. 3, pp. 203–233, 1999.

[3] R. L. Maurice and M. Bertrand, "Lagrangian speckle model and tissue motion estimation theory," *IEEE Trans. Med. Imag.*, vol. 18, no. 7, pp. 593–603, Jul. 1999.

[4] M. Lubinski, S. Emelianov, and M. O'Donnell, "Speckle tracking methods for ultrasonic elasticity imaging using short-time correlation," *IEEE Trans. Ultrason., Ferroelectr., Freq. Control*, vol. 46, no. 1, pp. 82–96, Jan. 1999.

[5] M. Lubinski, S. Emelianov, and M. O'Donnell, "Adaptive strain estimation using retrospective processing," *IEEE Trans. Ultrason., Ferroelectr., Freq. Control*, vol. 46, no. 1, pp. 97–107, Jan. 1999.

[6] E. S. Ebbini, "Phase-coupled two-dimensional speckle tracking algorithm," *IEEE Trans. Ultrason., Ferroelectr., Frequency Control*, vol. 53, no. 5, pp. 972–990, May 2006.

[7] E. E. Konofagou, T. Varghese, and J. Ophir, "Spectral estimators in elastography," *Ultrasonics*, vol. 38, no. 1–8, pp. 412–416, 2000.

[8] T. Varghese, E. E. Konofagou, J. Ophir, S. K. Alam, and M. Bilgen, "Direct strain estimation in elastography using spectral cross-correlation," *Ultrasound Med. Biol.*, vol. 26, no. 9, pp. 1525–1537, 2000.

[9] Y. Fung, *Biomechanics: Mechanical Properties of Living Tissues*, 2nd ed. New York: Springer, 1993, ch. 7.

[10] W. Yu, P. Yan, A. Sinusas, K. Thiele, and J. S. Duncan, "Towards pointwise motion tracking in echocardiographic images—Comparing the reliability of different features for speckle tracking," *Med. Image Anal.*, vol. 10, pp. 495–508, 2006.

[11] B. Jahne, H. Haussecker, and P. Geissler, *Handbook of Computer Vision and Applications*, 1st ed. New York: Academic, 1999, vol. 2, ch. 13.

[12] R. Szeliski, *Computer Vision: Algorithms and Applications*, 1st ed. New York: Springer, 2010, ch. 8.

[13] K. Kaluzynski, X. Chen, S. Emelianov, A. Skovoroda, and M. O'Donnell, "Strain rate imaging using two-dimensional speckle tracking," *IEEE Trans. Ultrason., Ferroelectr., Freq. Control*, vol. 48, no. 4, pp. 1111–1123, Jul. 2001.

[14] J. Luo, K. Fujikura, S. Homma, and E. E. Konofagou, "Myocardial elastography at both high temporal and spatial resolution for the detection of infarcts," *Ultrasound Med. Biol.*, vol. 33, no. 8, pp. 1206–1223, 2007.

[15] C. Pellot-Barakat, F. Frouin, M. Insana, and A. Herment, "Ultrasound elastography based on multiscale estimation of regularized displacement fields," *IEEE Trans. Med. Imag.*, vol. 23, pp. 153–163, Feb. 2004.

[16] H. Rivaz, E. Boctor, P. Foroughi, R. Zellars, G. Fichtinger, and G. Hager, "Ultrasound elastography: A dynamic programming approach," *IEEE Trans. Med. Imag.*, vol. 27, no. 10, pp. 1373–1377, Oct. 2008.

[17] H. Rivaz, E. M. Boctor, M. A. Choti, and G. Hager, "Real-time regularized ultrasound elastography," *IEEE Trans. Med. Imag.*, vol. 30, no. 4, pp. 928–945, Apr. 2011.

[18] F. Yeung, S. Levinson, D. Fu, and K. Parker, "Feature-adaptive motion tracking of ultrasound image sequences using a deformable mesh," *IEEE Trans. Med. Imag.*, vol. 17, no. 6, pp. 945–956, Dec. 1998.

[19] A. Elen, D. Loeckx, H. F. Choi, H. Gao, P. Claus, F. Maes, P. Suetens, and J. D'hooge, "3-d cardiac strain estimation using spatio-temporal elastic registration: In silico validation," in *Proc. IEEE Ultrason. Symp.*, Oct. 2007, pp. 1945–1948.

[20] A. Elen, D. Loeckx, J. Ganame, J. U. Voigt, P. Claus, J. D'hooge, and B. H. Amundsen, "3-d cardiac strain estimation using spatio-temporal elastic registration: In-vivo application," in *Proc. IEEE Ultrason. Symp.*, Nov. 2008, pp. 761–764.

[21] M. J. Ledesma-Carbayo, J. Kybic, M. Desco, A. Santos, M. Suhling, P. Hunziker, and M. Unser, "Spatio-temporal nonrigid registration for ultrasound cardiac motion estimation," *IEEE Trans. Med. Imag.*, vol. 24, no. 9, pp. 1113–1126, Sep. 2005.

[22] G. Piella, M. D. Craene, C. Yao, G. P. Penney, and A. F. Frangi, "Multiview diffeomorphic registration for motion and strain estimation from 3d ultrasound sequences," in *Proc. Int. Conf. Funct. Imag. Model. Heart*, 2011, vol. 2, pp. 375–383.

[23] J. Kybic and D. Smutek, "Computational elastography from standard ultrasound image sequences by global trust region optimization," in *Proc. Int. Conf. Inf. Process. Med. Imag.*, 2005, pp. 299–310.

[24] M. A. Lubinski, S. Y. Emelianov, K. R. Raghavan, A. E. Yagle, A. R. Skovoroda, and M. O'Donnell, "Lateral displacement estimation using tissue incompressibility," *IEEE Trans. Ultrason., Ferroelectr., Freq. Control*, vol. 43, no. 2, pp. 247–255, Mar. 1996.

[25] S. K. Alam and J. Ophir, "Reduction of signal decorrelation from mechanical compression of tissues by temporal stretching: Applications to elastography," *Ultrasound Med. Biol.*, vol. 23, no. 1, pp. 95–105, 1997.

[26] S. K. Alam, J. Ophir, and E. E. Konofagou, "An adaptive strain estimator for elastography," *IEEE Trans. Ultrason., Ferroelectr., Freq. Control*, vol. 45, no. 2, pp. 461–472, Mar. 1998.

[27] P. Chaturvedi, M. Insana, and T. Hall, "2-D companding for noise reduction in strain imaging," *IEEE Trans. Ultrason., Ferroelectr., Freq. Control*, vol. 45, no. 1, pp. 179–191, Jan. 1998.

[28] M. Insana, P. Chaturvedi, T. J. Hall, and M. Bilgen, "3-D companding using linear arrays for improved strain imaging," in *Proc. IEEE Ultrason. Symp.*, 1997, vol. 2, pp. 1435–1438.

[29] P. Chaturvedi, M. Insana, and T. Hall, "Testing the limitation of 2-D local companding in strain imaging using ultrasound," *IEEE Trans. Ultrason., Ferroelectr., Freq. Control*, vol. 45, no. 4, pp. 1022–1031, Jul. 1998.

[30] T. Liang and W. Yu, "A coupled filtering method to solve feature-motion decorrelation in speckle tracking," in *Proc. IEEE Int. Symp. Biomed. Imag.*, 2010, pp. 312–315.

[31] Y. Fung, *A First Course in Continuum Mechanics*, 2nd ed. Englewood Cliffs, NJ: Prentice-Hall, 1977.

[32] J. Prince and J. Links, *Medical Imaging Signals and Systems*, 1st ed. Englewood Cliffs, NJ: Pearson Prentice Hall, 2006, ch. 10,11.

[33] J. Meunier and M. Bertrand, "Echographic image mean gray level changes with tissue dynamics: A system-based model study," *IEEE Trans. Biomed. Eng.*, vol. 42, no. 4, pp. 403–410, Apr. 1995.

[34] J. Meunier, "Tissue motion assessment from 3-D echographic speckle tracking," *Phys. Med. Biol.*, vol. 43, pp. 1241–1254, 1998.

[35] F. M. J. Valckx and J. M. Thijssen, "Characterization of echographic image texture by cooccurrence matrix parameters," *Ultrasound Med. Biol.*, vol. 23, no. 4, pp. 559–571, 1997.

[36] J. Meunier and M. Bertrand, "Ultrasonic texture motion analysis: Theory and simulation," *IEEE Trans. Med. Imag.*, vol. 14, no. 2, pp. 293–300, Jun. 1995.

[37] J. Jensen, "A model for the propagation and scattering of ultrasound in tissue," *J. Acoust. Soc. Am.*, vol. 89, no. 1, pp. 351–353, 1991.

[38] S. K. Alam, J. Ophir, I. Cespedes, and T. Varghese, "A deconvolution filter for improvement of time delay estimation in elastography," *IEEE Trans. Ultrason., Ferroelectr., Freq. Control*, vol. 45, no. 6, pp. 1565–1572, Nov. 1998.

[39] R. L. Maurice, J. Ohayon, Y. Fretigny, M. Bertrand, G. Soulez, and G. Cloutier, "Noninvasive vascular elastography: Theoretical framework," *IEEE Trans. Med. Imag.*, vol. 23, no. 2, pp. 164–180, Feb. 2004.

[40] E. Mercure, G. Cloutier, C. Schmitt, and R. L. Maurice, "Performance evaluation of different implementations of the Lagrangian speckle model estimator for non-invasive vascular ultrasound elastography," *Med. Phys.*, vol. 35, no. 7, pp. 3116–3126, 2008.

[41] C. Schmitt, G. Soulez, R. Maurice, M. Giroux, and G. Cloutier, "Non-invasive vascular elastography: Toward a complementary characterization tool of atherosclerosis in carotid arteries," *Ultrasound Med. Biol.*, vol. 33, no. 12, pp. 1841–1858, 2007.

[42] R. L. Maurice, M. Daronat, J. Ohayon, E. Stoyanova, F. S. Foster, and G. Cloutier, "Non-invasive high-frequency vascular ultrasound elastography," *Phys. Med. Biol.*, vol. 50, no. 7, pp. 1611–1628, 2005.

[43] T. Zakaria, Q. Zhao, and R. L. Maurice, "Optical-flow-based b-mode elastography: Application in the hypertensive rat carotid," *IEEE Trans. Med. Imag.*, vol. 29, no. 2, pp. 570–578, Feb. 2010.

[44] J. Jensen, "Field: A program for simulating ultrasound systems," *Med. Biol. Eng. Comput.*, vol. 34, no. 1, pp. 182–191, 1996.

[45] J. Jensen and N. Svendsen, "Calculation of pressure fields from arbitrarily shaped, apodized and excited ultrasound transducers," *IEEE Trans. Ultrason., Ferroelectr., Freq. Control*, vol. 39, no. 2, pp. 262–267, Mar. 1992.